Intrusion rheology in grains and other flowable materials

Intrusion rheology in grains and other flowable materials

Hesam Askari,[1] Ken Kamrin,[1]

[1]*Massachusetts Institute of Technology, 77 Massachusetts Ave., Cambridge, MA 02139, USA*

Abstract — The interaction of intruding objects with deformable materials arises in many contexts, including locomotion in fluids and loose media, impact and penetration problems, and geospace applications. Despite the complex constitutive behaviour of granular media, forces on arbitrarily granular intruders are observed to obey surprisingly simple, yet empirical 'resistive force hypotheses'. The physics of this macroscale reduction, and how it might play out in other media, has however remained elusive. Here, we show that all resistive force hypotheses in grains arise from local frictional yielding, revealing a novel invariance within a class of plasticity models. This mechanical foundation, supported by numerical and experimental validations, leads to a general analytical criterion to determine which rheologies can obey resistive force hypotheses. We use it to explain why viscous fluids are observed to perform worse than grains, and to predict a new family of resistive-force-obeying materials, cohesive media such as pastes, gels and muds.

The interaction of solid objects with a surrounding, plastically-deforming media is a common aspect of many natural and man-made processes. In the animal world, when organisms undulate, pulse, crawl, burrow, walk, or run on loose terrain they implicitly deform their environment to produce propulsive reaction forces giving rise to their motion[1]. The physics of such interactions has been studied over a broad range of species, including aquatic organisms[2,3], small insects and lizards[4,5], as well as humans and other legged-mammals[6,7]. Similar principles are used for robotic applications to design machines that run[8], fly[9], swim[10], or walk in fluids or sand[11,12]. Such complex interactions are also key to modeling vehicular locomotion on granular substrates, excavation in sand and soil[13,14], and similar problems in extra-planetary conditions[15,16]. These topics and others, including cratering dynamics and penetration in plastic solids[17,18], all depend crucially on the way local material properties produce global resistive forces on arbitrary intruders.

Inspired by a related rule-set for swimming micro-organisms at low Reynolds numbers[10,19–21], a modified and wholly-empirical Resistive Force Theory (RFT) for granular materials has been proposed to estimate forces on intruding surfaces moving through granular media[5,22,23]. Its use in these experimental studies show that RFT is a very strong approximation in granular media, often stronger than the corresponding version for linear viscous fluids[24]. The simplicity of the method and its effectiveness are remarkable in light of the complex constitutive properties observed of granular matter, including nonlinearity, history-dependence, and nonlocality[25–29]. Being more of a hypothesis than a theory due to lack of a physical or mathematical explanation, new physics must be understood to explain how granular media, a complex system locally, is explained by such a simple rule-set globally.

Herein we show that granular RFT arises as a consequence of two of the most salient mechanical features of dry granular media: a frictional yield criterion and no cohesion. A continuum theory based on these hypotheses is implemented numerically to study many 2D and 3D intrusion cases and the results show rather conclusively that: (i) the continuum model quantitatively predicts existing experimental intrusion data and corresponding experimental RFT input data, (ii) the continuum model reproduces the surface-level superposition rules postulated by RFT on global bodies, and (iii) by comparing to analogous viscous flow problems, the fundamental superposition concept is stronger in the granular model. Then, by performing an analysis of our continuum system, we obtain an explanation as to why the RFT approximation is so strong in granular media and why it is less so for viscous fluids. In so doing we identify new fundamental RFT formulas, which relate the experimental RFT inputs to measurable properties like granular density, friction coefficient, and the gravitational acceleration, which could be exploited in experimentally challenging circumstances such as locomotion in micro-gravity. Our analytical approach leads to a general criterion to determine constitutive models capable of possessing an RFT-like reduction. To demonstrate this newfound capability, we use it to predict that purely cohesive media can also sustain a strong RFT. We then confirm this directly, using a set of full-scale finite-element simulations of intrusion in a cohesive yield stress fluid.

Background on Granular Resistive Force Theory

In recent experimental studies of arbitrarily-shaped intruders moving in granular beds, it was determined that the resistive force against intruder motion is rather well represented by a simple

superposition principle[23]; the intruder boundary can be decomposed into a connected collection of differential planar elements and the total resistive force is deemed equal to the sum of the resistive forces on each element *as if it were moving steadily on its own*. For concreteness, let us consider first the problem of an arbitrarily shaped quasi-2D intruder of thickness D buried in a granular bed; we will generalize this approach to 3D in the upcoming sections. Gravity points in the $\hat{z}$ direction, $z = 0$ represents the granular surface. Formally, a surface element is on the *leading surface* if a ray along its velocity vector does not intersect another point on the surface. For any subset S of the leading surface of the intruder, RFT is defined by the claim that when the body is moving in the xz-plane the resistive force (f_x, f_z) on S is well-approximated by

$$(f_x, f_z) = \int_S \big(\alpha_x(\beta,\gamma),\ \alpha_z(\beta,\gamma)\big)\ H(z)\ z\ dS \tag{1}$$

where β is the orientation angle (attack angle) of the differential surface element and γ is the angle of the velocity vector (intrusion angle) of the element, both measured from the horizontal. The key ingredient in RFT is the selection of the functions α_x and α_z, which is done experimentally from force data for small intruding flat plates under various γ and β conditions. The term $H(z)z$, for H the Heaviside function, removes resistive force above the free surface and increases the resistance linearly with depth.

The effectiveness **Eq. 1** is unexpected for many reasons. At first glance, it appears to be motivated by the assumption of a lithostatic pressure distribution, $\sigma_{ij} = -\rho g z \delta_{ij}$, surrounding the moving intruder. However, this assumption is strongly incorrect. DEM simulations of buried granular intruders[30], experimental data[31], as well as our own simulations (see Supplemental Materials) contradict this assumption rather significantly. Experiments show the stress on a moving intruder

deviates from lithostatic by as much as a factor of 30 in granular media[31]. The deviation from a linearly varying pressure field is pronounced everywhere the material is moving[31], and continues over a distance into the static zones (e.g. Supplemental Materials, **Fig. S2**). Additionally, the superposition property of **Eq. 1** assumes that the force on a segment of the leading surface depends only on its position, orientation, and motion direction, with no cross correlation of resistive forces whatsoever between the different segments. This is a significant unproven assumption and the major source of simplification in RFT. The strength of this assumption in grains is unexpected in light of the more de-localized nature of force and motion in other materials; in linearly viscous fluids, for example, the Stokeslet boundary integral formula requires that the motion at any point on a submerged surface depend on the resistive force distribution over the entire surface, weighted inversely by distance. For these reasons, the surprising accuracy of **Eq. 1** in practice has remained an open physical question since its introduction.

Frictional plastic rheology

To obtain deformation and stress within a continuous body of grains, we consider a constitutive behavior in line with the following basic assumptions: (i) We assume a constant internal friction coefficient, μ_c, to relate the scalar shear stress and pressure during plastic flow. (ii) We assume a rapid approach to the critical-state of volume-conserving flow[25] — granular dilation is typically only a few percent regardless — such that plastically flowing and rigid media are assumed to be at some close-packed density, ρ_c. (iii) We append an 'opening behavior' that lets material expand volumetrically (i.e. lets $\rho < \rho_c$) when an element attempts to enter a state of tension,

to model the cohesionless granular disconnection response. Open states often occur in the wake of a moving intruder, before material from above collapses back down to ρ_c as discussed in the Supplemental Information (Section **S1**) in detail. The bare-bones model we propose, with ρ_c and μ_c as the sole parameters, does not account for rate-sensitivity, evolving strength/porosity during flow, fabric anisotropy, or nonlocal effects based on particle size, which are all known to exist. The mathematical details of this model, which we shall refer to as *frictional plasticity*, are given next. The Supplemental Materials provides a discussion of the possible relevance of the other modeling complexities just mentioned.

Details of the continuum approach

The strain-rate tensor is defined from the spatial velocity field, v_i, by $D_{ij} = (\partial v_i/\partial x_j + \partial v_j/\partial x_i)/2$. We define the scalar (equivalent) shear-rate as $\dot{\gamma} = \sqrt{2D'_{ij}D'_{ij}}$ where $D'_{ij} = D_{ij} - \delta_{ij}D_{kk}/3$ is the strain-rate deviator. Assuming that the Cauchy stress, σ_{ij}, is co-directional with the strain-rate, and that the Drucker-Prager yield criterion is satisfied during yielding, we write

$$\sigma_{ij} = -P\delta_{ij} + 2\mu_c P D'_{ij}/\dot{\gamma} \quad \text{if} \quad \dot{\gamma}, P > 0. \tag{2}$$

In the above, $P = -\sigma_{kk}/3$ is the isotropic pressure. Whenever $\dot{\gamma}, P > 0$, we assert incompressible plastic flow ($D_{kk} = 0$) such that the density of the packing remains at ρ_c. Whenever $\rho < \rho_c$, we set $\sigma_{ij} = 0$ to represent granular disconnection. Momentum balance, $\partial\sigma_{ij}/\partial x_j + \rho g_i = \rho\dot{v}_i$, closes the system for arbitrary boundary value problems, where g_i is the acceleration of gravity and the superscript dot represents the material time derivative.

To provide stresses in rigid zones, where $\dot{\gamma} = 0$ and $P > 0$, and to aid in implementing the above pressure and flow constraints numerically, we admit a small elastic strain component to the deformation[32]. See the Supplemental Materials (section **S1**) for more details. As long as the elastic stiffness is sufficiently high, the observed plastic flow behavior is unaffected and approaches a rigid-plastic solution, a point we verified directly in our simulations.

We numerically implemented the model in 3D using a custom material model in the finite-element package Abaqus/Explicit[33] (see the Supplemental Materials **S1** for details; Material definition Code is also available as a Supplementary file). We first consider problems with plane-strain symmetry before considering general cases. No-penetration conditions are applied at the sides and bottom of the bed and the free surface is pressure-free. Gravity is gradually ramped up to its final value before intruder motion begins. The intruding object is represented as a fully rough, thin object. Sample flow directions and velocity distributions for a plate intruder obtained numerically by the continuum theory are shown in **Fig. 1** and compared to DEM results in the literature for the same geometry, having similar density and internal friction[22]. It is worthwhile to note that even though our intruder boundary condition assumes a fully rough interaction, which is an inexact representation of the condition assumed in the DEM simulation, the positive comparison suggests this difference is not crucial.

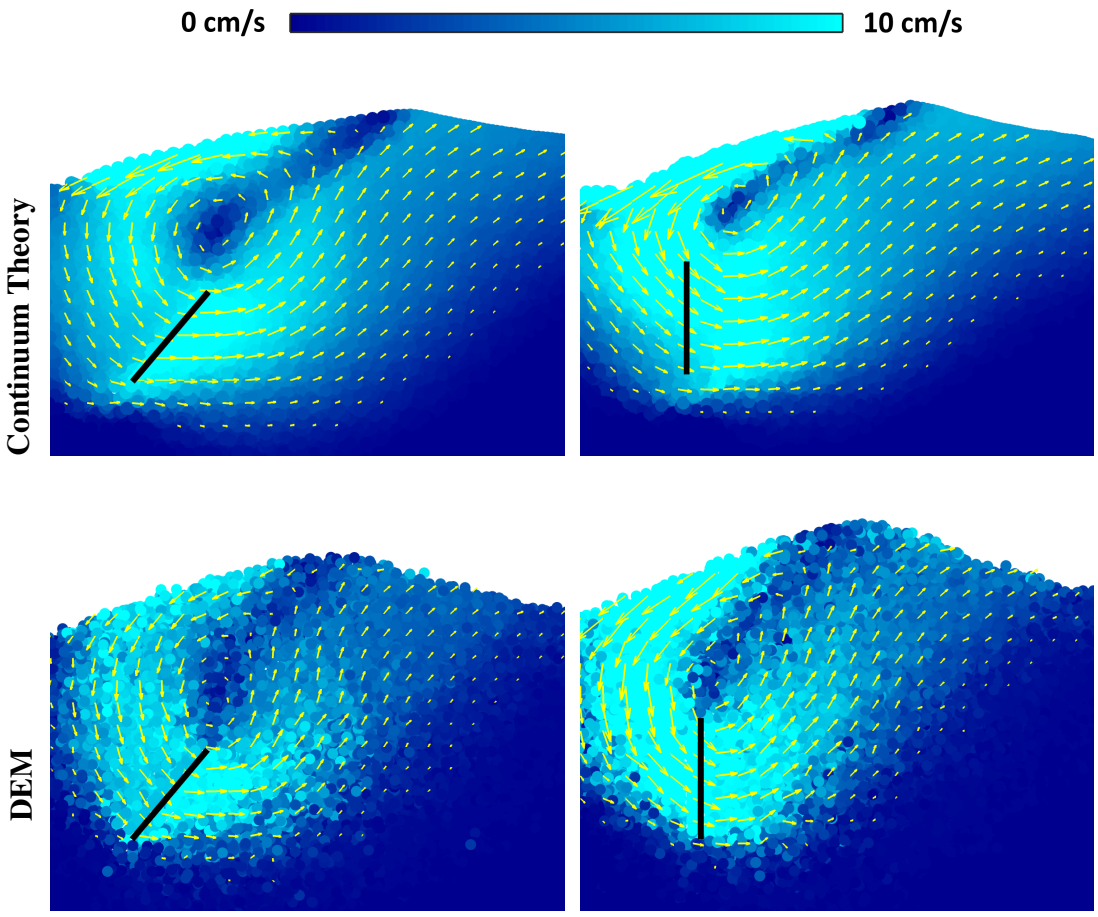

Figure 1 | **Theoretically predicted intrusion flow fields.** Speed distribution (contours) and velocity directions (arrows) created by motion of a submerged flat intruder moving rightward at 10 cm/s at two sample orientations. Results from the continuum theory (top row) and DEM simulations from the literature[22] (bottom row).

Results from the continuum theory

To establish a potential connection between frictional plasticity and RFT, we begin by simulating a flat intruder moving under many attack angles β and intrusion angles γ ($0 < \beta, \gamma < \pi$) to obtain

predictions for the resistive force plots (RFP's) of α_x and α_z. For each angle pair, the drag and lift forces acting on the plate are extracted when plastic flow is well-developed. To compare RFP's, we fit our continuum model parameters (μ_c and ρ_c) from reported properties of loose packed 0.3 mm glass beads[5]. As shown in **Fig. 2**, computed RFP's of α_x and α_z are strikingly similar to the experimentally obtained RFP's for glass beads[5]. The only noticeable difference between the two sets of figures is in the location of maximum drag force in the $\alpha_x^{\text{Continuum}}$ plot, which could be attributed to the oversimplification of assuming a no-slip intruder boundary condition. We reiterate that no fitting parameters were used in the constitutive model, only the reported repose angle and density of the experimental material[5].

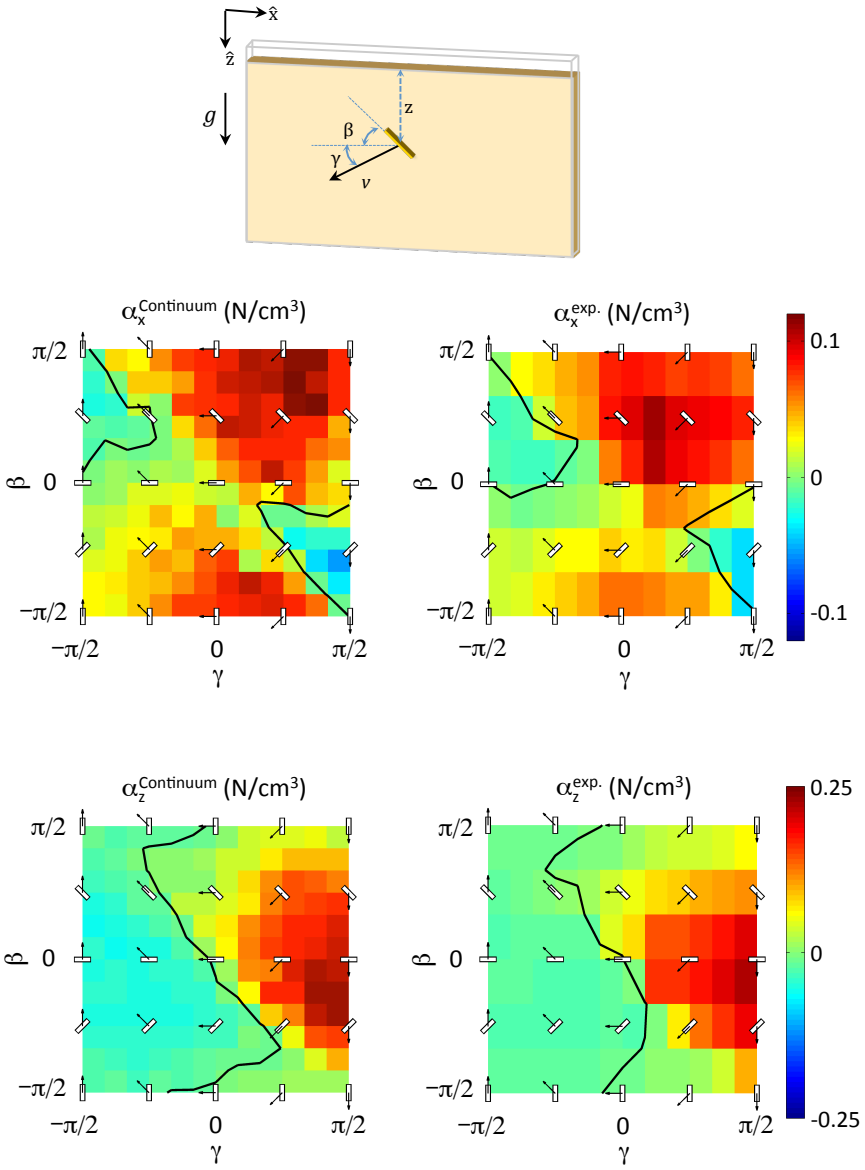

Figure 2 | Theoretically predicted vs experimentally obtained resistive force plots. RFP's obtained from frictional plasticity simulations ('Continuum' superscript), compared against published experimental RFP's[5] ('exp.' superscript) for a media composed of glass beads. α_x and α_z represent resistance coefficients in the x and z directions, respectively, γ and β are the attack angle and intrusion angle, respectively. Solid black lines show the zero values.

When the shape of the intruder is changed from plates to more arbitrary selections, we find the resistive forces obtained from the continuum theory comply very well with the superposition principle of RFT. For instance, in **Fig. 3**, the force distribution and resultant forces on circular- and diamond-shaped intruders are obtained directly from finite-element implementation of the frictional plastic model. The forces are then compared with the corresponding RFT predictions, which use the model-generated RFP's shown in **Fig. 2**. Though some errors are observed at the edges, the force distributions from both methods show a good match, and resultant force vectors show a near perfect correlation. This observation suggests that the deviations in force distributions may be due to numerical variations in the explicit finite element implementation of the theory.

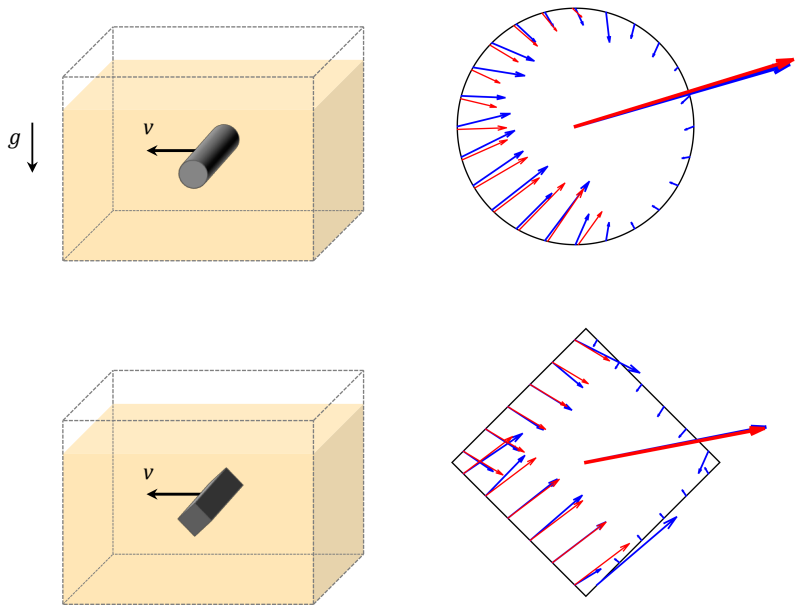

Figure 3 | Demonstration of the superposition principle arising from the continuum model. Distribution of force on the perimeter of two long moving objects as calculated directly from simulations of our continuum theory (→), compared to predictions from RFT using theoretical RFP's from Figure 2 (→).

Net resistive force shown at the center of the object; the two models give nearly indistinguishable results. Intruders move horizontally with speed v. Gravity g is oriented downward.

Eq. 1 can be extended naturally to general 3D cases, to include a non-trivial out-of-plane dimension; experiments[5] have verified that surfaces whose shapes vary in the y direction also maintain the superposition principle. To assess the generality of the RFT superposition principle in 3D, we employ our model to study forces on a sequence of buried V-shaped intruders. Because RFT is supposed to apply only to the leading surface of an intruder, we limit our attention to an obtuse V geometry, with apex angle fixed at $\theta_V = 135^\circ$, in which most orientations of the V admit both wings to be part of the leading surface.

We consider both vertically and horizontally aligned cases for the intruder orientation, varying the orientation angle φ of the submerged V over many values, where φ denotes a pitching angle (in vertical case) or yawing angle (in horizontal case), c.f. **Fig. 4(a)**. For each orientation, we impose rightward motion of the V intruder, and record the three-dimensional vector of resistive force that arises on the intruder at steady state. Then we run two new simulations, one for each wing of the intruder moving by itself, where the wing is simulated as a single plate maintaining the same exact alignment, positioning, and motion that it had when it partook in the group V motion. If RFT superposition holds, the sum of forces in the latter two tests should equal that of the full V test. In **Fig. 4(b)** we perform the same sequence of tests but assume instead a zero-Reynolds viscous fluid for the surrounding media, simulated using a similar finite-element code. All cases engage considerable drag force in the direction of motion, as expected. The vertically aligned

intruders experience vanishing F_y due to symmetry, and F_z switches sign at certain orientations due to the plowing action of the intruder movement, similar to the oscillatory nature of the y-force for the horizontal intruder. In the horizontal case, unlike the zero viscous F_z force, the intruder in the granular bed experiences an F_z force that on average pushes upward, demonstrating the well-known drag induced lift effect[22] in granular systems.

The comparison in **Fig. 4(a)** shows that superposition works extremely well in frictional plasticity for all force components. The agreement is roughly in the same range as the deviations observed in past granular RFT experiments[22,34]. In the ranges indicated in gray, the leading-surface assumption of RFT is violated; i.e. one plate is behind the other. The agreement is not as strong in these zones but still overall good. For this 3D study there are no analogous experimental tests in the literature to verify the findings of the theory. The error of the RFT force prediction, $|\mathbf{F}-\mathbf{F}_{RFT}|/|\mathbf{F}|$, is found to be 7.3% averaged over all orientations of the V and 3.9% when orientations that violate the leading-surface assumption are excluded.

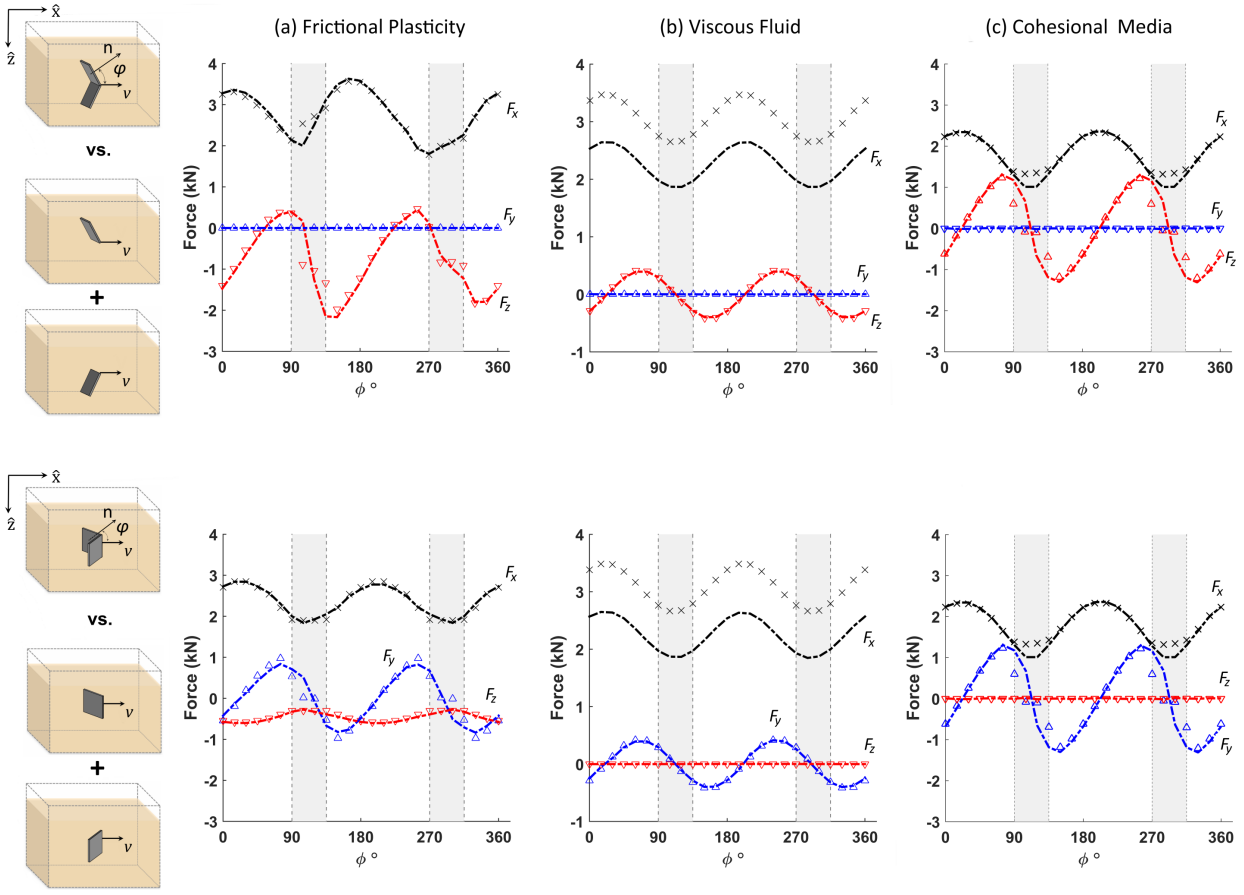

Figure 4 | Validity check for superposition in 3D. The drag force, F_x ($\times$), and the components of lift, F_z ($\bigtriangledown$), and lateral force, F_y ($\bigtriangleup$), acting on a submerged 'V' intruder moving rightward with speed v at various orientation angles, φ, with respect to the motion direction. Vertical (top row) and horizontal (bottom row) intruder alignments are both tested. Gravity g points down. Dashed lines show the corresponding forces obtained by superposition from isolated, individual-wing tests. Rheology of the surrounding media: [Left] Frictional plasticity (ρ_c=4g/cm^3, μ=0.4); [Center] Zero-Reynolds viscous fluid (ηv=15N/m); [Right] Purely cohesive media (τ_y=10 kPa). Intruder consists of two square plates of side length 20cm. Gray regions indicate orientations violating the leading-edge assumption of RFT.

In contrast, the superposition force in a viscous fluid half-space has a considerable error in the drag direction as shown in **Fig. 4(b)**, which is the largest force component. The total error of the force vector is about 36% averaged over all orientations. The nontrivial component in the lateral direction actually seems to show a good degree of superposition but this may be a coincidence; when the apex angle of the V is varied, the disagreement becomes more pronounced. In the presumably simpler case of $\theta_V = 180°$, i.e. a flat intruder, the error of viscous superposition has significant values in this component too, leading to an average error of 42%, while the superposition of the frictional model maintains its accuracy with an average error of about 4.6% (see Supplemental Materials, section **S4**)

Analytical explanation

The results thus far have demonstrated numerically that RFT hypotheses emerge strongly from the continuum equations of frictional plasticity. To provide an explanation as to *why* these equations replicate RFT and to predict if other materials have a strong RFT collapse, we study the behavior of resistive forces in a simple family of geometries reminiscent of a "garden hoe". Exact solutions to the continuum plasticity system are highly nontrivial to obtain, but in this geometry many results can be inferred using dimensional analysis without having to solve the differential equation system.

Consider a semi-infinite half-space of frictional continuum media (see **Fig. 5**). Suppose a large square-shaped intruder with edge length L is inserted into the media at angle β from the horizontal. Its top edge remains coincident with the free surface. The intruder is translated at a

speed v in a direction angled γ from horizontal, producing an assumed quasi-static motion of the material. The total resistive force $\mathbf{F}_{\text{gran}}$ on the intruder is then calculated from the continuum model. Due to the parameters of the model, the force can only depend on β, γ, L, μ_c, the weight density, $\rho_c g$, and perhaps a wall friction coefficient between the intruder and the material, μ_w. Define L, L/v and $\rho_c g L (L/v)^2$ as units of length, time, and mass, respectively. Non-dimensionalizing, we find that $\mathbf{F}_{\text{gran}} = \rho_c g L^3 \ \mathbf{\Psi}_{\text{gran}}(\beta, \gamma, \mu_c, \mu_w)$. Redefining $\mathbf{\Psi}_{\text{gran}}$ by absorbing the material constants, we have

$$\mathbf{F}_{\text{gran}} = L^3 \ \mathbf{\Psi}_{\text{gran}}(\beta, \gamma). \tag{3}$$

To approximate the same force using RFT, one first computes RFP's of α_x and α_z by gathering data on the intrusion of a small plate of edge length $\lambda \ll L$. The above formula can be applied to the small plate, and the result is that the RFP's must obey $\big(\alpha_x(\beta,\gamma), \alpha_z(\beta,\gamma)\big) = 2\mathbf{\Psi}_{\text{gran}}(\beta,\gamma)/\sin\beta$. We then check the RFT superposition principle by integrating **Eq. 1** over the surface, S, of the $L \times L$ garden hoe to obtain

$$\mathbf{F}^{\text{RFT}}_{\text{gran}} = \int_S \big(\alpha_x(\beta,\gamma), \alpha_z(\beta,\gamma)\big) \ z \ dS = \int_S \left(2\mathbf{\Psi}_{\text{gran}}(\beta,\gamma)/\sin\beta\right) \ z \ dS = L^3 \ \mathbf{\Psi}_{\text{gran}}(\beta,\gamma). \tag{4}$$

This formula is precisely that of **Eq. 3**. Likewise, RFT hypotheses agree with full frictional-plastic continuum model solutions in the garden hoe family of geometries. Additionally, we see that gravity and density can be lumped as a scaling constant in the vector function $\mathbf{\Psi}_{\text{gran}}$. This prediction that all resistive force plots scale linearly in $\rho_c g$ for fixed friction constant(s) was validated in additional finite-element simulations.

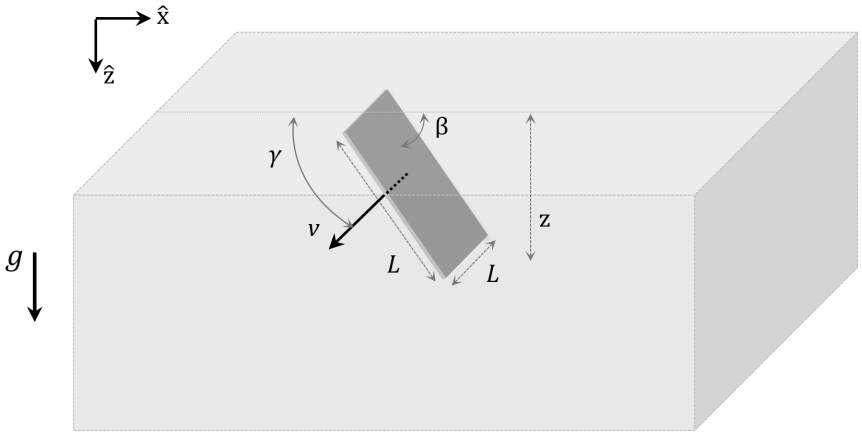

Figure 5 | Schematic of an RFT litmus test geometry. The 'garden hoe' geometry: An arbitrarily oriented square plate with side length L tilted at an angle β to the horizon with one edge at the free surface. It is set into motion in an arbitrary direction shown by velocity vector v oriented at angle γ to the horizon in a semi-infinite domain of material. Gravity vector g points downward and the bottom of the plate is located at depth z.

For comparison, consider instead a viscous fluid, which obeys the Stokes equations, $\eta\,\partial^2 v_i/\partial x_j^2 - \partial P/\partial x_i + \rho g_i = 0,\ \ \partial v_i/\partial x_i = 0$, for dynamic viscosity η. For the same garden-hoe geometry described above, the intrusion force, $\mathbf{F}_{\text{visc}}$, must depend on β, γ, v, L, and η. It cannot depend on ρg as this term can be removed by absorbing it into the pressure in the Stokes equations without altering the resultant intruder force. We choose $L, L/v$, and $\eta L^2/v^2$ as the length, time and mass units respectively, giving the dimensionless variables β, γ, and $\mathbf{F}_{\text{visc}}/\eta L v$. Consequently, in viscous media, the force on the intruder must have the form $\mathbf{F}_{\text{visc}} = \eta L v\ \mathbf{\Psi}_{\text{visc}}(\beta, \gamma)$ for some

vector-valued function $\mathbf{\Psi}_{\text{visc}}$. Absorbing the viscosity into $\mathbf{\Psi}_{\text{visc}}$, we have

$$\mathbf{F}_{\text{visc}} = L\, v\, \mathbf{\Psi}_{\text{visc}}(\beta, \gamma). \tag{5}$$

That the drag force grows linearly with L is similar to other Stokesian drag formulas; the drag on a sphere is proportional to its radius, for example.

We now compare the above form to a superposition-based solution, and determine if the two agree.[1] We suppose an isolated areal patch of small characteristic width λ oriented at various angles β and traveling at angles γ, and compute a local drag law. This takes the form $\{\text{Force/Area}\} = \big(a_x(\beta,\gamma), a_z(\beta,\gamma)\big)\ v$. Unlike the granular case, viscous rheology is pressure-insensitive, which is why the local drag rule is independent of depth. The formula for viscous drag, **Eq. 5**, implies that $\big(a_x(\beta,\gamma), a_z(\beta,\gamma)\big) = \mathbf{\Psi}_{\text{visc}}(\beta,\gamma)/\lambda$. The total force is then estimated by superposition of the local drag rule over the surface of the macroscopic geometry:

$$\mathbf{F}^{\text{RFT}}_{\text{visc}} = \int_S \big(a_x(\beta,\gamma), a_z(\beta,\gamma)\big)\ v\ dS = \frac{L^2}{\lambda} v\ \mathbf{\Psi}_{\text{visc}}(\beta,\gamma). \tag{6}$$

The result scales as L^2, but this is not correct; per **Eq. 5**, the actual force scales as L. The disagreement implies that the surface-superposition principle is not precise for viscous fluids. The difference manifests due to a non-removable factor of λ, the selected micro-size, showing up in the local drag rule. The same issue arises in the common 1D application of RFT, used for slender

[1] Unlike **Eq. 1**, the Resistive Force Theory of viscous fluids is historically an approximation developed for quasi-1D bodies only. To compare the effectiveness of frictional vs viscous superposition on surfaces, the analogous surface-level assumptions are considered here; we return to the 1D version of viscous RFT and compare to its frictional counterpart in the Supplemental Information (section **S2**).

bodies such as flagella and long micro-organisms. In the Supplemental Materials (section **S2**), we explain how the accuracy of granular RFT continues in the limit of a slender body, while the viscous case, by contrast, retains this small-scale geometrical dependence, taking the form of a well-known logarithmically growing error.

Going beyond viscous fluids and frictional media, the garden hoe analysis can be applied diagnostically to arbitrary flow models to predict new RFT's in other materials. For example, consider a purely cohesional, rate-independent media, which can be modeled as a non-Newtonian fluid whose viscosity takes the form $\tau_y/\dot{\gamma}$ for some constant yield stress τ_y. Such a model describes the flow of certain gels[35], pastes[36], and muds [37] when strain-rates are small-enough to neglect dependence of flow stress on $\dot{\gamma}$. In this material model, the intruder force can only depend on β, γ, L, and τ_y. We define L, L/v and $\tau_y L(L/v)^2$ as units of length, time, and mass, respectively. Non-dimensionalizing, we find $\mathbf{F}_{\text{coh}} = \tau_y L^2\ \mathbf{\Psi}_{\text{coh}}(\beta, \gamma, \tau_y)$. Redefining $\mathbf{\Psi}_{\text{coh}}$ by absorbing the material constants, we obtain $\mathbf{F}_{\text{coh}} = L^2\ \mathbf{\Psi}_{\text{coh}}(\beta, \gamma)$. We now write cohesive RFT and check if it agrees with this relation. Applying the previous relation to a small plate with length λ, the force per area must obey $\mathbf{F}_{\text{coh}}/\lambda^2 = 2\mathbf{\Psi}_{\text{coh}}(\beta, \gamma)/\sin\beta \equiv \big(\alpha_x(\beta, \gamma), \alpha_z(\beta, \gamma)\big)$. Superposing this local drag rule over the original $L \times L$ object gives

$$\mathbf{F}_{\text{coh}}^{\text{RFT}} = \int_S \big(\alpha_x(\beta, \gamma), \alpha_z(\beta, \gamma)\big)\ dS = L^2\ \mathbf{\Psi}_{\text{coh}}(\beta, \gamma). \tag{7}$$

The agreement between $\mathbf{F}_{\text{coh}}$ and $\mathbf{F}_{\text{coh}}^{\text{RFT}}$ means this material model has potential to possess a strong RFT. Our prediction is confirmed in V-intruder tests in **Fig. 4(c)**; the error of the RFT estimate, $|\mathbf{F} - \mathbf{F}_{RFT}|/|\mathbf{F}|$, is found to be 17% over the entire range orientations, and 2.8% when neglecting the orientations violating the leading edge requirement (in grey). The RFT in cohesional media

shown here has, to our knowledge, never previously been identified.

Outlook

The granular constitutive model we have used in this work was chosen to capture salient granular flow behaviors — a frictional, cohesionless constitutive relation — and we have shown that this bare description is sufficient to bring about RFT. Evidently there is more to the rheology of granular flow than these essential behaviors and there are certainly limits where additional effects can become significant. The Supplemental Materials, section **S3**, provides more discussion on how inclusion of effects such as rate-sensitivity, nonlocality, or stress-dilatancy may influence the superposition results. However, because the two essential properties used in our approach are still the foundations of these more detailed constitutive approaches, any additional effects from these sources, for intrusion problems in the typical regimes discussed in this paper, should be within the margin of error between our theoretically obtained RFP's and the experimentally reported values in the literature.

The analysis in the garden-hoe geometry appears to have utility as a litmus test to discern which rheologies can have a strong RFT. Finite-element implementations verify the predictions made by this analytical method as shown in **Fig. 4**. While it is certainly a necessary condition for strong RFT-type superposition in a material, the fact that RFT continues to work beyond the flat garden-hoe family, on surfaces with curves and kinks, may be related to *hyperbolicity* in the material's governing equations. For example, frictional (and cohesional) plasticity form a hyperbolic

system in space (in quasi-static 2D conditions), with stress characteristics extending from boundaries along 'slip-lines'[38]. This produces domains of dependence in the material such that stresses in certain zones can be attributed to the traction on a specific part of the surface of the intruder. This is in sharp contrast to viscous fluids, in which the equations are *elliptic*, and the stress at any point on an object's surface is influenced by the motion and shape of the object's entire boundary.

In much the same way the methods described herein have shown capable of predicting and confirming stronger or weaker RFT's in different materials, a major implication of the work is the possibility to identify and detail new RFT's in other flowable materials when new applications arise. As the garden hoe analysis is straightforward to apply, we have noticed other problem setups that pass the test and would be worthy of further investigation including intrusion in frictional plastic substrates tilted at an incline to gravity, which could have implications in modeling sidewinding up granular inclines[39], and intrusion through inviscid fluids, which draws potential similarities with assumptions made in the Blade Element Theory of rotors[40]. By nature of the reconciliation of RFT with mechanics, reverting to the mechanical foundation could be a useful tool in determining RFT input data (RFP's) in circumstances difficult to measure experimentally, such as intrusion in micro-gravity. It is also possible, through study of the underlying mechanics, that broader versions of RFT may exist in more general interaction problems between structures and flowable media, beyond intrusion geometries.

1 Supplementary Materials

The goal of these supplementary materials is to provide more details about the modeling techniques, background, and calculations presented in the main manuscript of this paper. We describe different components of the finite-element approach followed by a more detailed discussion of the dimensional analysis and further numerical demonstrations.

Granular RFT is inspired from a similar reduced order approximation for viscous fluids. Viscous RFT, also known as local drag theory, has been used to estimate for the speed of swimming micro-organisms at low Reynolds numbers[19] and to study mobility of cells[10,21]. Unlike its granular counterpart, viscous RFT is mathematically reconcilable, arising from an approximation in the Stokeslet integral form of the solution to the system. Despite its lack of a similar foundation, experimental tests of granular RFT have demonstrated surprising effectiveness in predicting resistive forces on, and consequent locomotion of, arbitrarily shaped bodies moving in granular materials[5,22,23], frequently achieving an accuracy higher than its viscous counterpart.

We next provide a detailed description of our proposed constitutive modeling approach implemented numerically using the finite-element method package Abaqus.

S1. Numerical solution procedure

Elasticity-augmented constitutive relation – As outlined in the main paper, the deformation behavior of the granular material is modeled using a non-hardening Drucker-Prager (DP) yield

criterion (constant μ_c). When implementing the model, we assume a small portion of the deformation is elastic, which closes the system mathematically in regions of non-flowing material, and provides a natural route to implementing the pressure constraints previously described. The model then takes the form of a simple hypo-elastic-plastic formulation. At any time, the deformation gradient F_{ij} is used to construct the velocity gradient $\partial v_i/\partial x_j = \dot{F}_{ik}F^{-1}_{kj}$, which is divided into a symmetric stretching component D_{ij} and anti-symmetric spin component W_{ij}. The dot represents the Lagrangian time derivative. The stretching is further decomposed into elastic and plastic parts $D_{ij} = D^e_{ij} + D^p_{ij}$. Denoting the elastic shear and bulk moduli of the granular material by G and K respectively, the constitutive relationship for the stress is established by a rate form of elasticity if material is in a dense state (i.e. $\rho \geq \rho_c$). Assuming the Jaumann rate, we have:

$$\begin{cases} \dot{\sigma}_{ij} - W_{ik}\sigma_{kj} + \sigma_{ik}W_{kj} = KD^e_{kk}\delta_{ij} + 2G(D^e_{ij} - D^e_{kk}\delta_{ij}/3), & \text{if } \rho \geq \rho_c \\ \sigma_{ij} = 0, & \text{if } \rho < \rho_c \end{cases} \tag{S1}$$

where σ_{ij} is the Cauchy stress as described in the main paper. The above relationship asserts the material is stress-free if density falls below the critical density ρ_c, indicating a disconnected or 'open' material state. While granular disconnection is a common occurrence in large flow processes, representing this phenomenon within a plastic flow rule is a relatively new proposition[41]. The Cauchy stress is further divided into a hydrostatic pressure part given by $P = -\sigma_{kk}/3$ and a deviatoric part $\sigma^{'}_{ij} = \sigma_{ij} + P\delta_{ij}$, which is used to define the equivalent shear stress, $\bar{\tau} = \sqrt{\sigma^{'}_{ij}\sigma^{'}_{ij}/2}$. The plastic strain-rate, D^p_{ij}, is uniquely defined to ensure the following conditions: (1) $D^p_{ij} = \lambda\sigma^{'}_{ij}$, (2) $\lambda = 0$ if $\bar{\tau} < \mu_c P$, (3) $\lambda > 0$ only if $\bar{\tau} = \mu_c P$, and (4) $\bar{\tau} \leq \mu_c P$. The next section details how this system of updates and constraints is implemented numerically.

Update step – Given the stress and deformation gradient at time t, σ_{ij}^{t} and F_{ij}^{t} respectively, as well as the new deformation gradient, $F_{ij}^{t+\Delta t}$, the goal is to obtain the updated stress $\sigma_{ij}^{t+\Delta t}$. We begin[41] by calculating the updated density $\rho^{t+\Delta t} = \rho^{t=0}/J$ where $J = \det(F_{ij}^{t+\Delta t})$ is the Jacobian. In all our simulations, we assume $\rho^{t=0} = \rho_c$; because we gradually ramp up gravity, the system begins as a granular assembly barely in contact and at zero pressure. If the deformed density is smaller than the critical density we set $\sigma_{ij}^{t+\Delta t} = 0$ according to **Eq. S1**. Otherwise, we proceed to obtain updated stress $\sigma_{ij}^{t+\Delta t}$ using a variant of the radial return algorithm[42] as we describe next.

We start by assuming a purely elastic step, i.e. $D_{ij}^{p} = 0$, under **Eq. S1**, which updates the stress to a "trial stress" state (σ_{ij}^{tr}). If the trial stress results in an equivalent shear stress $\bar{\tau}^{tr} = \sqrt{\sigma_{ij}^{tr'}\sigma_{ij}^{tr'}/2}$ that is less than $\mu_c P^{tr}$, it is accepted as the updated stress. If not, it is then adjusted by

$$\sigma_{ij}^{t+\Delta t} = \sigma_{ij}^{tr'}\mu_c P^{t+\Delta t}/\bar{\tau}^{tr} - P^{t+\Delta t}\delta_{ij}. \tag{S2}$$

Since $P^{tr} = P^{t+\Delta t}$ due to the isochoric plastic flow assumption, the effective shear stress $\bar{\tau}$ is seen to reduce following a constant pressure route to reside on the yield surface and $\sigma_{ij}^{t+\Delta t}$ is updated accordingly. This essentially represents usage of a tangent modulus to return the trial stress state σ_{ij}^{tr} back to the yield surface at the end of the increment[42].

Encoding the material model and geometric inputs – The constitutive relation is implemented as a custom VUMAT subroutine (See Supplementary file 'Granular-VUMAT.f') in the Abaqus finite element package. For problems in quasi-2D conditions, we use a one element thick bed of material with in-plane nodal constraints to ensure plane-strain motion. We model the intruder as

a rigid set within the body that moves at an assigned, constant rate. This choice relinquishes the need to define a complex contact routine between multiple objects, which would bring in additional contact parameters. This simplicity comes with the cost that the simulation conditions are not exactly the same as the experimental conditions used in the literature. We showed in the main paper that this assumption does not bring significant error compared to experimental data. To obtain $\alpha_x^{\text{Continuum}}$ and $\alpha_z^{\text{Continuum}}$, the same mesh is used for a given attack angle (β=constant) and only the direction of the intrusion angle γ is adjusted to minimize mesh effects. A similar approach is employed for the three-dimensionally varying flows in terms of the intruder representation. In these tests, the exact same mesh structure is used for horizontal and vertical V-shaped intruders to eliminate any attribute of mesh dependence.

Simultaneous dense and disconnected matter – In the case of a flat plate traveling within granular material, for example, one would expect free space to be created behind the intruder which is filled by material falling into the space from above. This process should cause reduced density in the trailing path of the intruder, which is clear in our simulations as shown in **Fig. S1**.

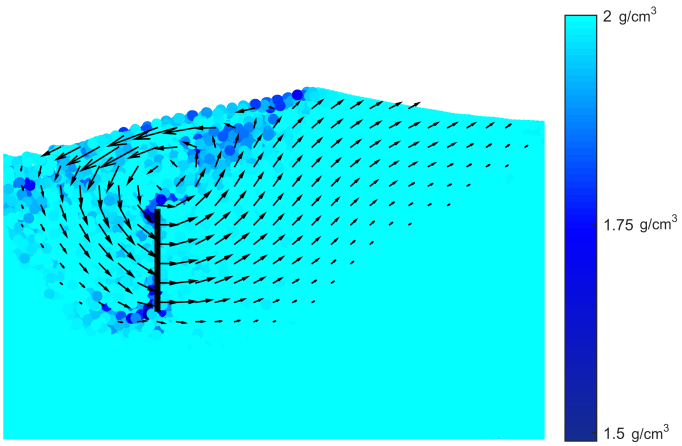

Figure S1 | Dense vs. open states. Plot of the local density in a granular bed using the frictional plasticity model, solved via FEM. The flat, vertical intruder is moving rightward. Densities below $\rho_c = 2$ g/cm^3 denote disconnected material in an 'open state'.

Pressure distribution in the granular bed – The pressure field in a static granular bed can match a lithostatic distribution in an initial, unperturbed, virgin state. As soon as the granular bed is disturbed with movement of an intruder, the pressure distribution undergoes a dramatic shift, as the stress field reorients based on the strain-rate field. Considerable localization of pressure has been shown to occur [30,31] similar to the results from our continuum model. **Fig. S2** shows two snapshots of the pressure distribution before and after movement of the intruder, showing the localization of pressure upon plastic deformation. The figure confirms that the granular stress field is non-lithostatic in an extended subregion containing the intruder, marked by a large stress concentration ahead of the intruder, and an approximately vanishing stress behind it.

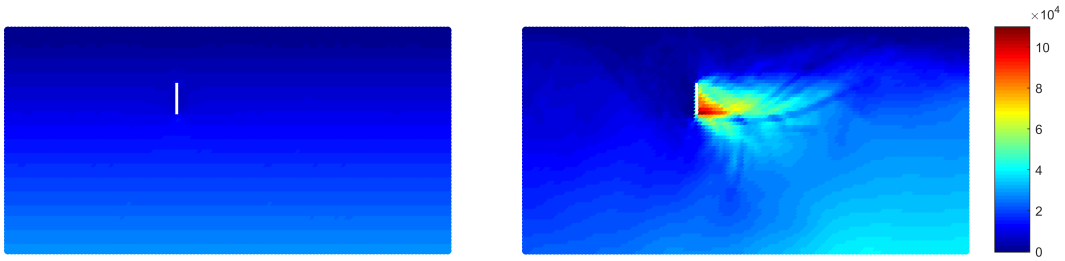

Figure S2 | Pressure distribution before and after rightward movement of an intruder. Intruder is 0.2m long buried at a depth of 0.3m simulated within a frictional plasticity finite-element model for glass beads. Pressure plotted in kPa.

S2. Resistive force theory for slender bodies

A surface-level form of RFT was presented in the main paper. Here, we analyze the more classical version applicable to slender bodies, which can be obtained as a cross-sectional integral of the surface-level form. In slender-body RFT, one assumes a velocity- and orientation-dependent local formula for the resistive force per length. In the granular case, the formula also contains depth-dependence [22]. The force per length can be computed from the drag on an isolated small segment, whose length is characteristic of small-scale motion in the whole; for example, the wavelength of an undulating swimmer [19].

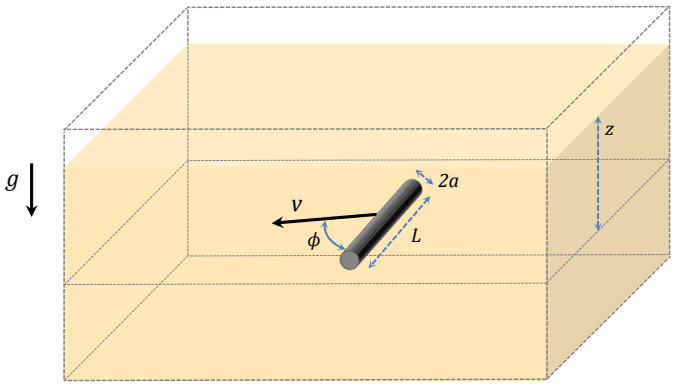

Figure S3 | Study of slender-body RFT on long rods. Schematic diagram.

The strength of the RFT superposition assumption can be studied in the case of a (neutrally buoyant) horizontal rod of length L and radius a, aligned (without loss of generality) in the x-direction, traveling horizontally with speed v in a direction ϕ from the tangent to the bar, as shown in **Fig. S3**. In viscous fluid, the force on such a rod is known to obey the classical Stokes drag formula

$$\mathbf{F}_{\text{visc}} \sim \frac{\eta v L}{\log L/a}\mathbf{c}(\phi) \tag{8}$$

for large L/a. To use RFT for the same problem, we can choose an isolated segment of length $\lambda < L$ as the reference length, use the above formula with length λ to calculate the force-per-length relation, and then use superposition to estimate the force on a bar of length L. One finds[19,43] the relative error of the RFT prediction grows $\sim \log(L/\lambda)$.

The reason for the logarithmic error relates to the fact that there is no 2D solution, finite at infinity, for Stokes flow around a circular obstacle, a result known as "Stokes' Paradox". Hence, long

rods never achieve a constant force-per-length independent of their length. Dimensional analysis explains this result[44]; a force-per-length variable in the 2D limit can only take the form

$$\mathbf{F}_{\text{visc}}/L = \eta v\ \mathbf{c}(\phi) \tag{S5}$$

which is contradictory — the formula purports that the drag force is independent of the body's radius a, even as $a \to 0$. This means that the force-per-length in viscous fluids is never L-independent.

In the case of a frictional media, there is no such paradox. Dimensionally, the force-per-length can depend on ϕ, a, v, the granular weight density, $\rho_c g$, the internal friction, μ_c, depth, z, and rod surface friction, μ_w. The dimensionless force-per-length $(\mathbf{F}_{\text{gran}}/L)/\rho_c g a^2$ is thus a function of the dimensionless inputs ϕ, μ_c, μ_w, L/z, and a/z, implying

$$\mathbf{F}_{\text{gran}}/L = \rho_c g a^2\ \mathbf{c}_{\text{gran}}(\phi, \mu_c, \mu_w, z/a). \tag{S3}$$

for some function $\mathbf{c}_{\text{gran}}$. This result has a physical dependence on a and corroborates our frictional plasticity simulations (see **Fig. 3** in the Main Text) and previous studies[45]. As such, as long as $L \gg a$, and one considers points further than $O(a)$ from the rod's ends, the force-per-length along the rod attains a uniform, constant value independent of L. Consequently, slender-body RFT in frictional media approaches the exact solution when applied to a long straight rod.

S3. The influence of additional granular constitutive phenomena on the reduction to RFT

We discuss how a more detailed granular constitutive model is likely to affect the collapse to RFT. Rate-dependence in granular rheology arises through a rate-sensitive coefficient of friction $\mu_c(I)$

where the inertial number is $I = \dot{\gamma} d/\sqrt{P/\rho_s}$ with $\dot{\gamma}$ the shear-rate, d the particle diameter, P the pressure, and ρ_s the solid grain density. Generally speaking, when this number is larger than ~ 0.1 the the variation of μ_c with I is non-negligible[46]. Defining units of length, time and mass as L, L/v and $\rho_c g L^3/v^2$ respectively, we revisit our dimensional analysis of the garden hoe test and arrive at an additional dimensionless group $I_G = v^2 d^2/gL^2$ that accounts for inertial effects. Similarly, one could also include particle size-effects in the constitutive behavior, to account for the local strengthening of material that can occur if boundary features are small. This could become non-negligible when d/L is greater than ~ 0.1 [27,47]. Supposing size- and rate- dependent phenomena are included in the rheology and the problem is in a regime where either or both of these effects could matter, dimensional analysis of the garden hoe test instructs us to expect an extended general answer of the form

$$\mathbf{F}_{\text{gran}} = \rho_c g L^3 \mathbf{\Psi}_{\text{gran}} \left(\mu_c, \mu_w, b, \beta, \gamma, \frac{v^2 d^2}{gL^2}, \frac{d}{L} \right). \tag{S6}$$

Upon selecting a small reference length λ, the above formula yields an RFP relation $(\alpha_x, \alpha_z) = 2\mathbf{\Psi}_{\text{gran}}(\beta, \gamma, \frac{v^2 d^2}{g\lambda^2}, \frac{d}{\lambda})/\sin\beta$. Superposing this result over the garden-hoe surface, the RFT result is

$$\mathbf{F}^{\text{RFT}}_{\text{gran}} = \rho_c g L^3 \mathbf{\Psi}_{\text{gran}} \left(\mu_c, \mu_w, b, \beta, \gamma, \frac{v^2 d^2}{g\lambda^2}, \frac{d}{\lambda} \right). \tag{S7}$$

The lingering dependence of the superposition results on λ within the arguments of $\mathbf{\Psi}_{\text{gran}}$ could potentially cause the RFT prediction of (S7) to differ from the exact answer in (S6). Note that if I_G is large enough to affect $\mathbf{\Psi}_{\text{gran}}$, α_x and α_z will depend explicitly on the speed, contrary to the rate-independent RFP's that arise in the main text of the paper.

One could also include history and state-variable dependence in the constitutive model. Con-

trary to our simplifying assumption of a single value of μ_c, the packing fraction Φ is known to influence the internal friction coefficient, and the two variables obey a coupled evolution before material reaches a steady state of constant-volume shearing, known as the critical state[25]. Critical state models can be written that attempt to model the evolution of these two variables and capture the salient behaviors of granular flow above and below the critical state packing fraction, Φ_c^{ss}. A stress-dilatancy critical-state framework can be imposed[48,49], a particularly straightforward one of which is a coupled system of the form

$$\mu_c = \mu_c^{ss} + (\Phi - \Phi_c^{ss})\chi \tag{9}$$

$$\frac{d\Phi}{dt} = -(\Phi - \Phi_c^{ss})\Phi\chi\dot{\gamma} \tag{10}$$

where χ is a dimensionless constant and μ_c^{ss} is the friction coefficient at the critical state packing fraction. Note that if the packing fraction is above Φ_c^{ss} the material experiences shear-weakening under (constant-pressure) shearing; initially $\mu_c > \mu_c^{ss}$ and μ_c summarily decreases to μ_c^{ss} during flow. The opposite occurs if Φ is initially less than Φ_c^{ss}. These flow strength dynamics cause the character of flow in dense material to have qualitative differences compared to flows in loose material. Shear-weakening behavior is well-known to lead to flow instabilities in the form of shear bands, whereas shear-strengthening materials invoke smooth flow features. This may explain the appearance of force fluctuations and unsteady flow behavior during intrusion in densely prepared materials, and the comparatively smaller fluctuations in loose grains[12,50].

Even so, the garden-hoe test gives insight into why initially loose or dense granular systems both tend to obey RFT superposition, at least in a time-averaged sense. In view of the geometric

setup of this test from the main text, suppose an arbitrarily oriented square plate of width L is quasi-statically driven through a bed of stress-dilatant media at some initial packing fraction Φ_i. The time-averaged intrusion force, $\mathbf{F}_{\text{gran}}$, can depend only on L, v, β, γ, μ_w, $\rho_s g$, Φ_i, Φ_c^{ss}, μ_c^{ss}, and χ, where $\rho_s g$ is the weight density of a single grain. Nondimensionalizing yields,

$$\mathbf{F}_{\text{gran}} = \rho_s g L^3 \mathbf{\Psi}_{\text{gran}} \left(\mu_c^{ss}, \Phi_c^{ss}, \mu_w, \Phi_i, \chi\right). \tag{11}$$

Because all the arguments of $\mathbf{\Psi}_{\text{gran}}$ are independent of L and the prefactor goes as L^3, as was the case in our simple frictional plasticity model, then in exactly the same manner as in the frictional plasticity analysis the stress-dilatant material model will have a perfect correspondence between $\mathbf{F}_{\text{gran}}$ and the RFT-superposition value based on data from smaller plates.

S4. 3D superpositions tests in flat geometries

In the main paper, we evaluated the validity of the superposition principle in frictional media and viscous fluid for a V-shaped intruder. In this section we repeat the study for 'straight V'. The procedure is exactly similar to what was described in the main paper. **Fig. S4** shows the resistive forces found by superposition of two individual plates versus the actual resistive force for a twice longer flat plate. The norm of the error in the frictional case is 6.5 % which is similar to what was found for V-shape intruder. The same geometry in a viscous fluid shows a norm of error about 42%. Interestingly, the V-shaped intruder shown previously has smaller lateral force.

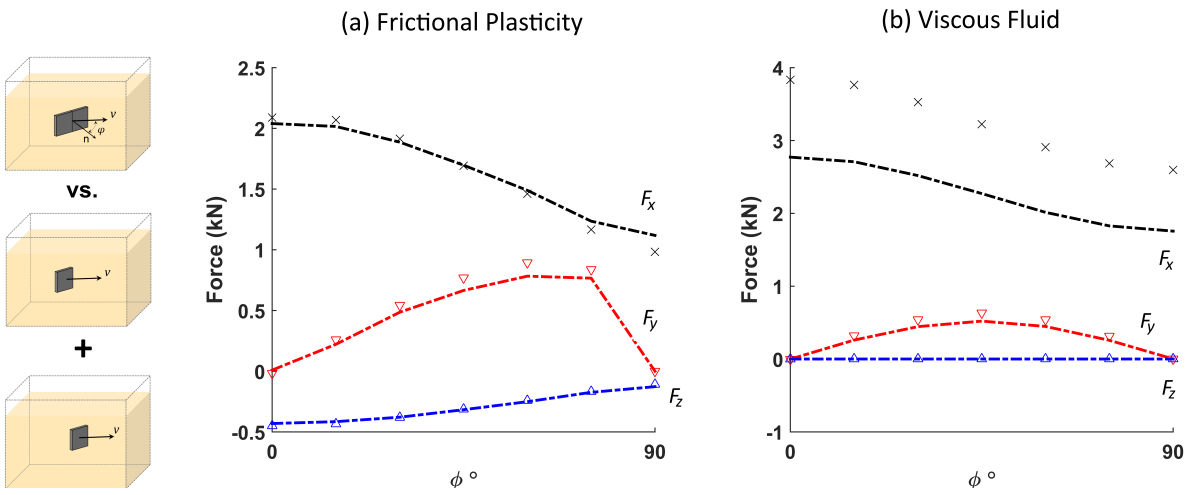

Figure S4 | Evaluation of superposition for a flat intruder. Finite-element results for the drag force, F_x, acting on a rightward moving submerged flat intruder ($\times$), and the components of lift, F_z ($\bigtriangledown$), and lateral force, F_y ($\bigtriangleup$), compared with superposition values (dashed) at various orientation angles, φ, for horizontal intruder alignments in (a) frictional media (left, $\rho_c = 4\text{g/cm}^3$, μ =0.4) and (b) viscous fluid (right, ηv=15N/m). Intruder consists of two square plates of side length 20cm at a depth of 60cm.

References

1. Dickinson, M. H. *et al.* How animals move: an integrative view. *Science* **288**, 100–106 (2000).

2. Vogel, S. *Life in moving fluids: the physical biology of flow* (Princeton University Press, 1996).

3. Lauder, G. V., Nauen, J. C. & Drucker, E. G. Experimental hydrodynamics and evolution: function of median fins in ray-finned fishes. *Integrative and Comparative Biology* **42**, 1009–1017 (2002).

4. Wang, Z. J. Dissecting insect flight. *Annu. Rev. Fluid Mech.* **37**, 183–210 (2005).

5. Li, C., Zhang, T. & Goldman, D. I. A terradynamics of legged locomotion on granular media. *Science* **339**, 1408–1412 (2013).

6. Thorpe, S. K., Holder, R. & Crompton, R. Origin of human bipedalism as an adaptation for locomotion on flexible branches. *Science* **316**, 1328–1331 (2007).

7. Biewener, A. A. Biomechanics of mammalian terrestrial locomotion. *Science* **250**, 1097–1103 (1990).

8. Bhushan, B. Biomimetics: lessons from nature–an overview. *Philosophical Transactions of the Royal Society of London A: Mathematical, Physical and Engineering Sciences* **367**, 1445–1486 (2009).

9. Ma, K. Y., Chirarattananon, P., Fuller, S. B. & Wood, R. J. Controlled flight of a biologically inspired, insect-scale robot. *Science* **340**, 603–607 (2013).

10. Williams, B. J., Anand, S. V., Rajagopalan, J. & Saif, M. T. A. A self-propelled biohybrid swimmer at low reynolds number. *Nature communications* **5** (2014).

11. Ijspeert, A. J., Crespi, A., Ryczko, D. & Cabelguen, J.-M. From swimming to walking with a salamander robot driven by a spinal cord model. *Science* **315**, 1416–1420 (2007). URL `http://www.sciencemag.org/content/315/5817/1416.abstract`. `http://www.sciencemag.org/content/315/5817/1416.full.pdf`.

12. Maladen, R. D., Ding, Y., Li, C. & Goldman, D. I. Undulatory swimming in sand: subsurface locomotion of the sandfish lizard. *science* **325**, 314–318 (2009).

13. Bekker, M. G. Off-the-road locomotion. *Research and development in Terramechanics* (1960).

14. Meirion-Griffith, G. & Spenko, M. An empirical study of the terramechanics of small unmanned ground vehicles. In *Aerospace Conference, 2010 IEEE*, 1–6 (IEEE, 2010).

15. Johnson, L. & King, R. Measurement of force to excavate extraterrestrial regolith with a small bucket-wheel device. *Journal of Terramechanics* **47**, 87–95 (2010).

16. Wong, J. Predicting the performances of rigid rover wheels on extraterrestrial surfaces based on test results obtained on earth. *Journal of Terramechanics* **49**, 49–61 (2012).

17. Uehara, J., Ambroso, M., Ojha, R. & Durian, D. Low-speed impact craters in loose granular media. *Physical review letters* **90**, 194301 (2003).

18. Shergold, O. A. & Fleck, N. A. Mechanisms of deep penetration of soft solids, with application to the injection and wounding of skin. In *Proceedings of the Royal Society of London A: Mathematical, Physical and Engineering Sciences*, vol. 460, 3037–3058 (The Royal Society, 2004).

19. Gray, J. & Hancock, G. The propulsion of sea-urchin spermatozoa. *Journal of Experimental Biology* **32**, 802–814 (1955).

20. Lighthill, J. *Mathematica Biofluiddynamics* (SIAM, 1975).

21. Lauga, E. & Powers, T. R. The hydrodynamics of swimming microorganisms. *Reports on Progress in Physics* **72**, 096601 (2009).

22. Ding, Y., Gravish, N. & Goldman, D. I. Drag induced lift in granular media. *Physical Review Letters* **106**, 028001 (2011).

23. Maladen, R. D., Ding, Y., Umbanhowar, P. B., Kamor, A. & Goldman, D. I. Mechanical models of sandfish locomotion reveal principles of high performance subsurface sand-swimming. *Journal of The Royal Society Interface* **8**, 1332–1345 (2011).

24. Rodenborn, B., Chen, C.-H., Swinney, H. L., Liu, B. & Zhang, H. Propulsion of microorganisms by a helical flagellum. *Proceedings of the National Academy of Sciences* **110**, E338–E347 (2013).

25. Schofield, A. & Wroth, P. Critical state soil mechanics (1968).

26. Kamrin, K. Nonlinear elasto-plastic model for dense granular flow. *Int. J. Plasticity* **26**, 167–188 (2010).

27. Kamrin, K. & Koval, G. Nonlocal constitutive relation for steady granular flow. *Phys. Rev. Lett.* **108**, 178301 (2012).

28. Henann, D. L. & Kamrin, K. A predictive, size-dependent continuum model for dense granular flows. *Proceedings of the National Academy of Sciences* **110**, 6730–6735 (2013).

29. Chen, W.-F. *Limit analysis and soil plasticity* (Elsevier, 2013).

30. Guillard, F., Forterre, Y. & Pouliquen, O. Depth-independent drag force induced by stirring in granular media. *Physical review letters* **110**, 138303 (2013).

31. Brzinski III, T., Mayor, P. & Durian, D. Depth-dependent resistance of granular media to vertical penetration. *Physical review letters* **111**, 168002 (2013).

32. Hill, R. New horizons in the mechanics of solids. *Journal of the Mechanics and Physics of Solids* **5**, 66–74 (1956).

33. Dassault Systèmes Simulia, Providence, RI. *Abaqus Reference Manuals*, 6.11 edn. (2011).

34. Goldman, D. I. Colloquium: Biophysical principles of undulatory self-propulsion in granular media. *Reviews of Modern Physics* **86**, 943 (2014).

35. Kinloch, I. A., Roberts, S. A. & Windle, A. H. A rheological study of concentrated aqueous nanotube dispersions. *Polymer* **43**, 7483–7491 (2002).

36. Senff, L., Labrincha, J. A., Ferreira, V. M., Hotza, D. & Repette, W. L. Effect of nano-silica on rheology and fresh properties of cement pastes and mortars. *Construction and Building Materials* **23**, 2487–2491 (2009).

37. Dzuy, N. Q. & Boger, D. V. Yield stress measurement for concentrated suspensions. *Journal of Rheology (1978-present)* **27**, 321–349 (1983).

38. Nedderman, R. M. *Statics and kinematics of granular materials* (Cambridge University Press, 2005).

39. Marvi, H. *et al.* Sidewinding with minimal slip: Snake and robot ascent of sandy slopes. *Science* **346**, 224–229 (2014).

40. Adkins, C. N. & Liebeck, R. H. Design of optimum propellers. *AIAA paper* 83–0190 (1983).

41. Dunatunga, S. & Kamrin, K. Continuum modeling and simulation of granular flows through their many phases. *Journal of Fluid Mechanics* **779**, 483–513 (2015).

42. Simo, J. C. & Taylor, R. L. Consistent tangent operators for rate-independent elastoplasticity. *Computer methods in applied mechanics and engineering* **48**, 101–118 (1985).

43. Lighthill, J. Flagellar hydrodynamics. *Siam Review* **18**, 161–230 (1976).

44. Happel, J. & Brenner, H. *Low Reynolds number hydrodynamics: with special applications to particulate media*, vol. 1 (Springer Science & Business Media, 2012).

45. Zhang, T. & Goldman, D. I. The effectiveness of resistive force theory in granular locomotion. *Physics of Fluids (1994-present)* **26**, 101308 (2014).

46. da Cruz, F., Emam, S., Prochnow, M., Roux, J.-N. & Chevoir, F. Rheophysics of dense granular materials: Discrete simulation of plane shear flows. *Physical Review E* **72**, 021309 (2005). URL `http://link.aps.org/doi/10.1103/PhysRevE.72.021309`.

47. Kamrin, K. & Henann, D. L. Nonlocal modeling of granular flows down inclines. *Soft matter* **11**, 179–185 (2015).

48. Wood, D. M. *Soil behaviour and critical state soil mechanics* (Cambridge university press, 1990).

49. Roux, S. & Radjai, F. Texture-dependent rigid-plastic behavior. In *Physics of dry granular media*, 229–236 (Springer, 1998).

50. Gravish, N., Umbanhowar, P. B. & Goldman, D. I. Force and flow transition in plowed granular media. *Physical review letters* **105**, 128301 (2010).

Acknowledgements K. Kamrin and H. Askari gratefully acknowledge support from Army Research Office Grants W911NF-14-1-0205 and W911NF-15-1-0196.

Author Contributions K.K. conceived the study and supervised the project. H.A. developed the computational routines and conducted the numerical modeling. K.K. and H.A. jointly performed the analysis and wrote the paper.

Competing Interests The authors declare that they have no competing financial interests.

Correspondence Correspondence and requests for materials should be addressed to K. Kamrin (email: kkamrin@mit.edu).